Evaluation of methods for connecting InSAR to a terrestrial reference frame in the Latrobe Valley, Australia

P. J. Johnston[1], M. S. Filmer[1], T. Fuhrmann[2]

1. School of Earth and Planetary Sciences & The Institute for Geoscience Research, Curtin University, GPO Box U1987, Perth WA 6845, Australia
2. National Geodesy Section, Geoscience Australia, GPO Box 378, Canberra ACT 2601, Australia (now at GNSS Performance Team, Airbus Defence & Space, Munich, Germany)

Corresponding author: Paul Johnston paul.j.johnston@curtin.edu.au

ORCIDs: P. J. Johnston (0000-0001-8605-0620), M.S. Filmer (0000-0002-3555-4869), T. Fuhrmann (0000-0001-7194-7486)

Abstract
Deformation measurements from satellite-borne synthetic aperture radar interferometry (InSAR) are usually measured relative to an arbitrary reference point (RP) of assumed stability over time. For InSAR rates to be reliably interpreted as uplift or subsidence, they must be connected to a defined Earth-centred terrestrial reference frame (TRF), usually made through GNSS continuously operating reference stations (CORS). We adapt and compare three methods of TRF connection proposed by different studies which we term the single CORS RP (SCRP), plane-fit multiple CORS (PFMC), and the multiple CORS RP (MCRP). We generalise equations for these methods, and importantly, develop equations to propagate InSAR and GNSS uncertainties through the transformation process. This is significant, because it is important to not only estimate the InSAR uncertainties, but also to account for the uncertainties that are introduced when connecting to the CORS to better inform our interpretation of the deformation field and the limitation of the measurements. We then test these methods using Sentinel-1 data in the Latrobe Valley, Australia. These results indicate that differences among the three TRF connection methods may be greater than their estimated uncertainties. MCRP appears the most reliable method, although it may be limited in large study areas with sparse CORS due to long wavelength errors and that gaps and/or steps may appear at the spatial limit from the CORS. SCRP relies on the quality of the single CORS connection, but can be validated by unconnected CORS in the study area. The PFMC method is suited to larger areas undergoing slow, constant deformation covering large spatial extents where there are evenly distributed CORS across the study area. Selecting an optimal method of TRF connection is dependent on local site conditions, CORS network geometry and the characteristics of the deformation field. Hence, the choice of TRF connection method should be carefully considered, because different methods may result in significantly different transformed deformation rates. We confirm slow subsidence across the Latrobe Valley relative to the vertical component of the ITRF2014, with localised high subsidence rates near open cut mining activities. Subsidence of ~ -6mm/yr is observed in the adjacent coastal region which may exacerbate relative sea level rise along the coastline, increasing future risks of coastal inundation.

Keywords: InSAR, GNSS, terrestrial reference frame, error propagation, datum connection, coastal subsidence.

1. Introduction

Satellite-borne synthetic aperture radar interferometry (InSAR) observations provide high resolution spatial coverage of ground motion in the off-nadir direction of the line of sight (LOS) of the SAR satellite. However, the LOS displacement from these processed data are differential within the extent of the scene. That is, the deformation is relative to the pixel(s) within the SAR scenes used as the reference point (RP), so is dependent on the uncertainty in the RP pixels, and their stability over time. Many InSAR studies adopt an RP in a region of assumed zero motion. However, if the assumed zero-motion RP is in fact undergoing unidentified horizontal or vertical land motion (VLM), then all other displacements in the scene relative to this RP will be misrepresented, and their true physical motion may be misinterpreted. A worst-case scenario is when subsidence is misinterpreted as uplift, and vice versa (e.g., Bui et al. 2020), a situation that can become more complex if the RP is undergoing non-linear VLM when it is assumed to be either stable, or undergoing linear motion only (e.g., Raucoules et al. 2013; Chang and Hanssen 2016).

To fully analyse and interpret land deformation from InSAR, the displacement results must be referred to a known Terrestrial Reference Frame (TRF; e.g., ITRF2014; Altimimi et al. 2016). This facilitates the consistent analysis of VLM in global and regional settings for geophysical phenomena such as tectonic studies (e.g., Hammond et al. 2018), ground water extraction (Bell et al. 2008), and monitoring tide gauge and coastal stability for global sea level studies (e.g., Brooks et al. 2007; Wöppelmann et al. 2013; Bekaert et al. 2017; Poitevin et al. 2019; Filmer et al. 2020). As well as referencing InSAR displacements in a TRF, there are numerous other error sources that can propagate into the InSAR-derived deformation, including tropospheric delay (e.g., Williams et al. 1998; Bekaert et al. 2015a; 2015b; Cao et al, 2018. Murray et al. 2019), long-wavelength ionospheric biases (e.g., Gomba et al. 2017; Fattahi et al. 2017), and orbit bias (e.g., Bähr and Hanssen 2012; Fattahi and Amalung 2014). These InSAR errors are in addition to those associated with connecting to the TRF, which is most commonly made through continuously operating GNSS stations (referred to herein as continuously operating reference stations; CORS), whose 3D positions are expressed with respect to a TRF. In this study, we transform the rates estimated from the InSAR time series (rather than the time series themselves), so as to mitigate the noise associated with individual InSAR acquisitions or GNSS daily positions (e.g., Mahapatra et al. 2018). The TRF connection errors can be divided into the following three components that can propagate through the TRF connection and contaminate the transformed InSAR rates: (1) uncertainty in the InSAR rate estimation at the RP; (2) uncertainty due to differences in time series between the InSAR rate estimation at the RP and the InSAR rate estimation at any other pixel in the scene; and (3) uncertainty in the GNSS rate estimation at the single (or multiple) CORS. The uncertainties and biases in the TRF itself (e.g., Collilieux et al. 2014; Riddell et al. 2017) are generally less than 1 mm/yr and are not considered here in TRF connection errors.

In this study, we assume that the connection must be made using InSAR pixels where the radar is backscattered from the natural or man-made features surrounding the CORS. This is the most commonly encountered situation, although alternatives (where available) are radar transponders (e.g., Mahapatra et al. 2014) fixed to the CORS structure as in Mahapatra et al. (2018), or corner reflectors (CRs) with a known connection to the CORS structure (e.g., Dheenathayalan et al. 2016; Parker et al. 2017; Fuhrmann et al. 2018). In these cases, the stable, high intensity signal from the transponder or CR is identified within the SAR scene and can be connected with higher accuracy (e.g., Mahapatra et al. 2014; Garthwaite 2017). However, transponders have not been widely used due to limited availability and costs, and the installation of CRs can be problematic given their size and shape and a

potential need for monitoring by repeat ground survey. A method for InSAR connection to a global TRF was suggested by Parker et al. (2019) where ties could be made to very long baseline interferometry (VLBI) antenna across land masses separated by ocean. However, this is not practical for local or regional studies because global distribution of VLBI antennas is sparse (e.g., there are only three VLBI stations in Australia).

There have been a number of methods used for TRF (or datum) connection. These vary in terms of the three steps for TRF connection, which require (1) determination of the InSAR RP rate (local spatial interpolation); (2) transformation of the InSAR RP rate to the GNSS rate at the CORS; and (3) transformation to multiple CORS where these are available within the InSAR extent. For example, Mahapatra et al. (2018) transform InSAR rates from an arbitrary 'free' datum to a TRF using the S-transform of Baarda (1981). In Mahapatra et al. (2018), a radar transponder (e.g., Mahapatra et al. 2014) is co-located with (i.e., physically fixed to) a CORS, so that the 3D position of the single InSAR pixel representing the transponder is known within the TRF. The transformation parameters computed between the GNSS and RP (transponder) pixel time series is applied to all InSAR pixels in the arbitrary datum. The method of Chang and Hanssen (2016) was used to mitigate the RP noise where the noise specific to the RP pixel time series (but not common across all pixels) is removed from all pixels following the transformation. An example was shown in Mahapatra et al. (2018) where InSAR time series from multiple RADARSAT-2 scenes processed over the Netherlands were transformed from the InSAR free datum to the RP from a transponder attached to a CORS co-located with a tide gauge station. The method of Mahapatra et al. (2018) was adapted by Filmer et al. (2020) where there was no transponder or CR in place, with a modification to handle a square array of >827,000 X-band pixels, and using the Create, Analysis Time series software (CATS; Williams 2008) to estimate rates and account for InSAR noise. Filmer et al. (2020) connected InSAR to a single GNSS CORS, using two additional CORS to verify the single CORS TRF connection.

Fuhrmann et al. (2015) used a two-step approach to datum connection, where the processed C-band (ERS and Envisat) InSAR persistent scatterers (PS; e.g., Ferretti et al. 2001; Kampes 2006; Hooper et al. 2007) were interpolated to levelling benchmarks and CORS. The vertical offset and spatial trend for the InSAR linear vertical rates were estimated from historical repeat levelling at benchmarks (Fuhrmann et al. 2014), with CORS used to estimate only the horizontal (east, north) offset and trend for the 3D velocities computed from the ascending and descending LOS InSAR PS. The vertical offset and trend were computed as a rate in mm/yr per 100 km, which assumed that the trend was the result of long-wavelength InSAR errors, primarily orbital error, and ionospheric effects. The levelling velocities were used for vertical constraint because they were considered more precise over a much longer time period (~100 years) than the CORS vertical velocities.

An alternative method for TRF connection was used by Bekaert et al. (2017) where six CORS in the US coastal region of Hampton Roads, Virginia, USA were used to reference historic ALOS-1 (L-band) InSAR (acquired 2007-2011) to the NA12 plate reference (Hammond et al. 2016). This study investigated coastal subsidence, and chose to reference only InSAR PS within 20 km of each of the six CORS because L-band atmospheric errors beyond this distance become too large (e.g., Fattahi et al. 2017). By limiting the PS distance from the CORS, the long-wavelength L-band errors are filtered out. Tying the 20 km radius of PS to six individual CORS was considered preferable to fitting a plane to the multiple CORS, as this may not properly account for variable ionospheric noise. Each CORS RP connection was referenced to at least 50 PS within 500 m. PS rates in overlapping radii from different CORS were estimated by weighted average.

Hammond et al. (2018) used levelling, tide gauges, GNSS and InSAR in their study of vertical land motion (VLM) in southern California. The GNSS imaging algorithm (Hammond et al. 2016) was used to estimate and remove rate differences among data sets, resulting in a grid of weighted median VLM values based on the closest neighbouring CORS so that the field is a function of the CORS network spacing that retains discontinuities rather than smoothing based on an assumed spatial distance. The GNSS imaging algorithm from Hammond et al. (2016) was also used to connect the GNSS rates to levelling benchmarks that were generally not co-located. To tie the LOS InSAR to the GNSS rates, the 3D GNSS rates were transformed into the radar LOS at each CORS using the InSAR incidence angle at the specific CORS location.

To determine the relative advantages and disadvantages of the different TRF connection methods, we test three adaptations of those discussed, then present generalised equations for the TRF connection steps and derive their error propagation for the uncertainty components in Section 2. We do not test the method of Hammond et al. (2018) because this requires a dense array of CORS which we do not have in our study area (Section 3). The three methods we test are:

1. Single CORS RP (SCRP): This method is based on that of Mahapatra et al. (2018) where the InSAR is connected at one CORS, applying a uniform transformation across the scene. Other CORS available within the SAR extent can be used to validate the single connection. This method is suited to limited area studies of <50 km from the CORS RP, and is adapted for where there are no transponders or CRs available (cf., Filmer et al. 2020; and Section 4 this article). Fuhrmann et al. (2018) implemented a variation of this method with ascending and descending SAR scenes to compute the rigorous conversion to VLM.
2. Plane fit to multiple CORS (PFMC): This method applies a planar transformation and can be employed where there are at least three CORS available. The relative InSAR observations are held fixed relative to each other, but forced to a best fit plane to all available CORS. This is the same as the method adopted by Fuhrmann et al. (2015) which was well-suited to the small magnitude long period linear deformation rates in that study area.
3. Multiple CORS RP (MCRP): Applies a transformation that varies at each CORS so as to avoid fitting as a rigid plane across the full scene. This method adopts multiple single CORS RPs within the SAR extent and can be considered a compromise between methods 1 and 2. For this method, we adapt that of Bekaert et al. (2017).

While it is assumed that rates from a long, uninterrupted CORS time series will be more reliable than the InSAR-derived relative displacement rates, it is often unclear what errors are introduced when the InSAR rates are transformed into the TRF using the CORS rates; specifically, how do we account for the errors in the GNSS and InSAR rate at the RP? The TRF transformation may introduce an error into relative InSAR rates that results in a possible bias when constrained at multiple CORS. Alternatively, constraining at one CORS implicitly trusts the phase ramp estimate that is computed from the InSAR stack and then used as a correction for long-wavelength orbit (cf. Fattahi and Amelung 2014) and ionospheric errors (cf. Fattahi et al. 2017; Gomba et al. 2017; Liang et al. 2019).

We will describe these three TRF connection methods, including how the different uncertainty components propagate into the final InSAR rates through the transformation so as to realise rates with associated uncertainties that account for different sources of error. To test this in a

practical sense, we will use ~2.7 years of processed Sentinel-1 data in the Latrobe Valley region of Australia. The purpose of this study is to test the relative advantages and disadvantages of these methods, and their TRF propagated uncertainties so as to guide InSAR users as to the most suitable method for their particular situation. An additional motivation for this experiment is to determine methods that can be used to develop a deformation model for use with national datums and reference frames, as suggested by Fuhrmann et al. (2018), and the optimal methods of combining InSAR and CORS in situations where there are limitations on the available data and infrastructure. Through these experiments, we present results and discussion on the land deformation occurring in this region. This extends to apparent subsidence along the adjacent coastline of south east Australia that may have the effect of exacerbating sea level rise (cf. Brooks et al. 2007; Mazzotti et al. 2008, Featherstone et al. 2015). This highlights the significance of not only transforming to a known TRF, but also being aware of the uncertainties of the transformed rates, and that using different transformation methods may result in different rates.

2. Methods

In this section, we set out the three methods listed in Section 1 (SCRP, PFMC, MCRP) to transform LOS InSAR data to a TRF. We do not discuss the InSAR processing method in this section (see e.g., Hanssen 2001), but consider that the input InSAR data for these methods are LOS post-processed deformation time series. The post-processed InSAR time series used for this study are output from the Stanford Method of Persistent Scatterers (StaMPS; Hooper 2008; Hooper et al. 2012), which are described in Section 3.1. The methods here result in transformed InSAR LOS rates, with the method to convert to vertical land motion (VLM) described in Section 2.4. The reader should assume all InSAR rates in this paper are LOS, unless otherwise stated.

2.1 Local spatial interpolation of InSAR to the RP

The first step in connecting InSAR to the TRF is to estimate the LOS InSAR rate (v_i^I) for each pixel across the scene in the InSAR reference frame. Then we identify the v_i^I near the RP that best represents the motion of the CORS pillar supporting the GNSS antenna (v_0^I) to which the TRF connection will be made. This is generalised as

$$v_0^I = \sum_{i \in N_0} w_i v_i^I \qquad (1)$$

where N_0 is a set of pixels in the neighbourhood of the RP (e.g., all points within a distance d). The weights should satisfy $0 \leq w_i \leq 1$, so that $\sum_{i \in N_0} w_i = 1$.

There are a number of ways to estimate v_0^I. These include adopting the rate of the nearest pixel (e.g., Mahapatra et al. 2018; Filmer et al. 2020), in which case both $|N_0|$ (the number of elements in N_0) and $w_i = 1$ in Eq. (1), or interpolating the rates from a number of pixels around the RP so that $|N_0| > 1$ in Eq. (1). When using v_i^I from multiple pixels, the average or median v_i^I of all pixels within a set distance (radius) of the RP can be used, or alternatively the radius can be determined on a case by case basis to take into account the different characteristics for each RP (see Section 3.2). Fuhrmann (2016) uses ordinary kriging (OK) to determine the weights w_i and the uncertainty in the derived rate v_0^I. Bekaert et al. (2017) uses the bootstrap method to interpolate to the RP in the MCRP method by taking random samples of pixels within 500 m of the RP, so that v_0^I is the mean of all the random samples. The MCRP uncertainty in v_0^I is computed as the standard deviation (SD) of those means, so is actually the SD of the mean and is therefore less than the uncertainties for other methods. This may lead to the uncertainty being under-estimated for the

MCRP (cf. Table 1). Note that the uncertainty for the RP spatial interpolation using multiple pixels is only used to assess the quality of the estimation for v_0^I (e.g., Section 3.2). For the purposes of propagating uncertainties through the TRF, we adopt the uncertainty from the InSAR rate estimation of v_0^I (σ_0^I) and not the uncertainty of the spatial interpolation to the RP. This is because we assume that v_0^I is representing the same motion as the CORS pillar.

2.2 Transformation for single RP and error propagation

The second step in the TRF connection is to estimate the 3D GNSS linear rates (east, north, up) in the TRF at the CORS, solving for annual and semi-annual terms (e.g., Blewitt and Lavallée 2002), spectral index (e.g., Williams 2003a) and any offsets due to changes in the receiver antenna or processing methodologies at known times (e.g., Williams 2003b). These 3D GNSS rates are then rigorously converted to the LOS rate (e.g., Fuhrman and Garthwaite 2019) in the TRF (v^G) using the incidence angle (θ) and the satellite heading (α) of the InSAR sensor. This avoids converting the InSAR rates to the GNSS vertical rate, which requires the assumption of no relative horizontal motion (Fuhrman and Garthwaite 2019).

The SCRP transformation (T_i^{SCRP}) is computed from a single CORS RP as

$$T_i^{SCRP} = v^G - v_0^I \tag{2}$$

A visual example of this transformation at a CORS is shown in the results (Section 3.1) in Figure 2. This transformation is applied to all pixels in the SAR scene so that the SCRP transformed rate (v_i^{SCRP}) is

$$v_i^{SCRP} = v_i^I - v_0^I + v^G \tag{3}$$

The uncertainties propagating through the SCRP transformation are shown here as variance

$$\left(\sigma_i^{SCRP}\right)^2 = \left(\sigma\left(v_i^I - v_0^I\right)\right)^2 + (\sigma^G)^2 = \left(\sigma_i^I\right)^2 + (\sigma_0^I)^2 - 2C\left(v_i^I, v_0^I\right) + (\sigma^G)^2 \tag{4}$$

$C(\cdot,\cdot)$ is covariance, $\left(\sigma_i^I\right)^2$ is the variance of v_i^I which is estimated for each pixel's time series. $\left(\sigma\left(v_i^I - v_0^I\right)\right)^2$ is the variance from estimating the linear rate of the difference between each InSAR pixel's time series (used to compute v_i^I) and the RP time series (used to compute v_0^I). $\left(\sigma\left(v_i^I - v_0^I\right)\right)^2$ increases with distance from the RP (where $\left(\sigma\left(v_i^I - v_0^I\right)\right)^2 = 0$) until there is no correlation between v_i^I and v_0^I (so that $\left(\sigma\left(v_i^I - v_0^I\right)\right)^2 \approx \left(\sigma_i^I\right)^2 + (\sigma_0^I)^2$). $(\sigma^G)^2$ is the variance of v^G at the RP and applied as a constant across the scene (e.g., Figure 5 (top right)).

2.3 Regional spatial interpolation – multiple RPs

In study areas where there are three or more evenly spaced CORS, it is possible to apply the PFMC method as follows. Let $d_j = v_j^G - v_{0,j}^I$ be the difference between GNSS and InSAR rates at the j^{th} CORS, with variance $\sigma_j^2 = \left(\sigma_j^G\right)^2 + \left(\sigma_{0,j}^I\right)^2$, and $P_{0,j} = (P_{0,j}^E, P_{0,j}^N)$ are the east and north co-ordinates of the CORS station provided in a conventional planar coordinate system. The difference between v^G and v_0^I can be modelled as follows:

$$T_i^{PFMC} = \beta_0 + \beta_E\left(P_i^E - \overline{P^E}\right) + \beta_N(P_i^N - \overline{P^N}) \tag{5}$$

The location $\bar{P} = (\overline{P^E},\ \overline{P^N})$ is the average position of all pixels in the InSAR scene. The model parameters $\beta^{plane} = (\beta_0 \quad \beta_E \quad \beta_N)^T$ are the transformation components to LOS rate at $\bar{P}$ and the dependence of the transformation on east and north coordinate. They are obtained by weighted least squares regression (e.g., Press et al. 1986)

$$\beta^{plane} = (X^T \Sigma\, X)^{-1} X^T \Sigma d \tag{6}$$

where $\Sigma = diag(1/\sigma_j^2),\ j = 1,2,..,N_{RP}$, with N_{RP} the number of RPs and the j^{th} row of X is $(1 \quad P_j^E - \overline{P^E} \quad P_j^N - \overline{P^N})$. The covariance matrix of the model parameters is $C_\beta = (X^T \Sigma\, X)^{-1}$. The total variance of the transformed InSAR rates $\left(\sigma_i^{PFMC}\right)^2$ is approximated by adding the variance of the InSAR rates $\left(\sigma_i^I\right)^2$ to the variance due to the model. i.e.,

$$\left(\sigma_i^{plane}\right)^2 = (1 \quad P_i^E - \overline{P^E} \quad P_i^N - \overline{P^N}) C_\beta (1 \quad P_i^E - \overline{P^E} \quad P_i^N - \overline{P^N})^T$$

$$\left(\sigma_i^{PFMC}\right)^2 = \left(\sigma_i^{plane}\right)^2 + \left(\sigma_i^I\right)^2 \tag{7}$$

This assumes independence of v_i^I from β^{plane} which is true for the entire scene except for locations within a few hundred metres of each CORS where the errors may be over-estimated. A minimum requirement to apply this method is three CORSs that are not collinear.

A second approach to transforming v_i^I to multiple GNSS CORS sites, the MCRP (method 3 in Section 1), is to limit the region where the TRF connection applies to a specified radius from each CORS (Bekaert et al. 2017). The specified distance may be based on the sensitivity of a sensor wavelength to long-wavelength errors, particularly ionospheric errors. According to Fattahi et al. (2017), L-band InSAR should be restricted to a 20 km limit to avoid large magnitude long-wavelength ionospheric errors (as in Bekaert et al. 2017), with C-band limited to ~85 km, and X-band to ~155 km. Where multiple CORS sites are within these distances, a spatially variable weighted sum (a_{ij}) of the transformation from each CORS site is applied for the overlapping regions. The variance of the transformed deformation in such regions is reduced because there is more than one transformation value. The MCRP transformation (T_i^{MCRP}) is defined as

$$T_i^{MCRP} = \sum_j a_{ij} d_j, \qquad a_{ij} = \frac{1/\sigma_{i,j}^2}{\left(\sum_j \frac{1}{\sigma_{i,j}^2}\right)} \tag{8}$$

where the summations are over all CORS sites within a given distance of the j^{th} RP . The variance due to the j^{th} RP (cf. Eq. (4) for $\left(\sigma_i^{SCRP}\right)^2$) is

$$\sigma_{i,j}^2 = \left(\sigma\left(v_i^I - v_{0,j}^I\right)\right)^2 + \left(\sigma_j^G\right)^2 \tag{9}$$

Following the MCRP transformation, v_i^I in the TRF is computed as

$$v_i^{MCRP} = v_i^I + T_i^{MCRP} \tag{10}$$

and the variance is calculated as

$$\left(\sigma_i^{MCRP}\right)^2 = \left(\sigma\left(v_i^I - \sum_j a_{ij} v_{0,j}^I\right)\right)^2 + \sum_j a_{ij} \left(\sigma_j^G\right)^2 \tag{11}$$

This method can only be applied to pixels within the scene that are within the specified radius of at least one CORS RP, with the radius dependent on the InSAR frequency band. While this method takes advantage of v^G from all CORS available in the study area, it also generates discontinuities in the transformation and errors at the edges of the disk-shaped regions around the RPs. Finally, if only one RP is within range, $a_{ij} = 1$, then the MCRP equations (8) and (11) become the SCRP equations (2) and (4).

2.4 Conversion from LOS to vertical

The vertical rate is usually of more practical interest than the InSAR LOS rate and so a further step is required to estimate VLM from the LOS rates. When redundant InSAR viewing geometries are available, e.g., ascending and descending orbits, the vertical and east-west deformation rates can be rigorously resolved, although north-south deformation is less well resolved due to the near polar satellite orbits (cf. Fialko et al. 2001; Wright et al. 2004). When there is only one SAR satellite orbit available (i.e., ascending or descending) the InSAR LOS cannot be rigorously converted to the vertical component. In these cases, other geodetic constraints on horizontal motion can be applied, or zero horizontal motion can be assumed, but this assumption should be clearly stated, and if possible, supported by geological or other geodetic information (e.g., Fuhrmann and Garthwaite 2019).

Where the vertical v_i^I can be rigorously computed, conversion from LOS to vertical rates is given by

$$v_U = (\tan\theta\cos\alpha \quad -\tan\theta\sin\alpha \quad \sec\theta) \cdot (v_E \quad v_N \quad v_{LOS}) \tag{12}$$

When only single pass LOS InSAR is available, and in the absence of any other horizontal rate information, the horizontal rates are assumed to be zero, and the vertical rate computed in Eq. (12) reduces to the approximate equation:

$$v_U = v_{LOS}\sec\theta \tag{13}$$

3. Case study in the Latrobe Valley, Australia

In this section, we apply three different methods of TRF connection (i.e., (1) SCRP, (2) PFMC, (3) MCRP) to Sentinel-1 data for the Latrobe Valley in southeast Australia (Figure 1) for the period 2 December 2015 to 25 June 2018 (decimal years 2015.92 - 2018.57). We compare the results from these methods, discussing their advantages and disadvantages within this study area.

Our study of the Latrobe Valley follows one of the wider Gippsland Basin by Ng et al. (2015) using ALOS PALSAR data from 2007-2011. Their study found localised high magnitude subsidence reaching -82 mm/yr in the Latrobe Valley that they attribute to above ground mining activities and associated mine dewatering. We will investigate this localised deformation for the years 2015.92 – 2018.57, but will connect our InSAR rates to ITRF2014-Aus, which is ITRF2014 with the horizontal Australian plate motion removed using the Australian Plate model published in ICSM (2017). This is a standard TRF used in Australia which is fixed horizontally with respect to the Australian continent. ITRF2014-Aus has the same vertical component as ITRF2014.

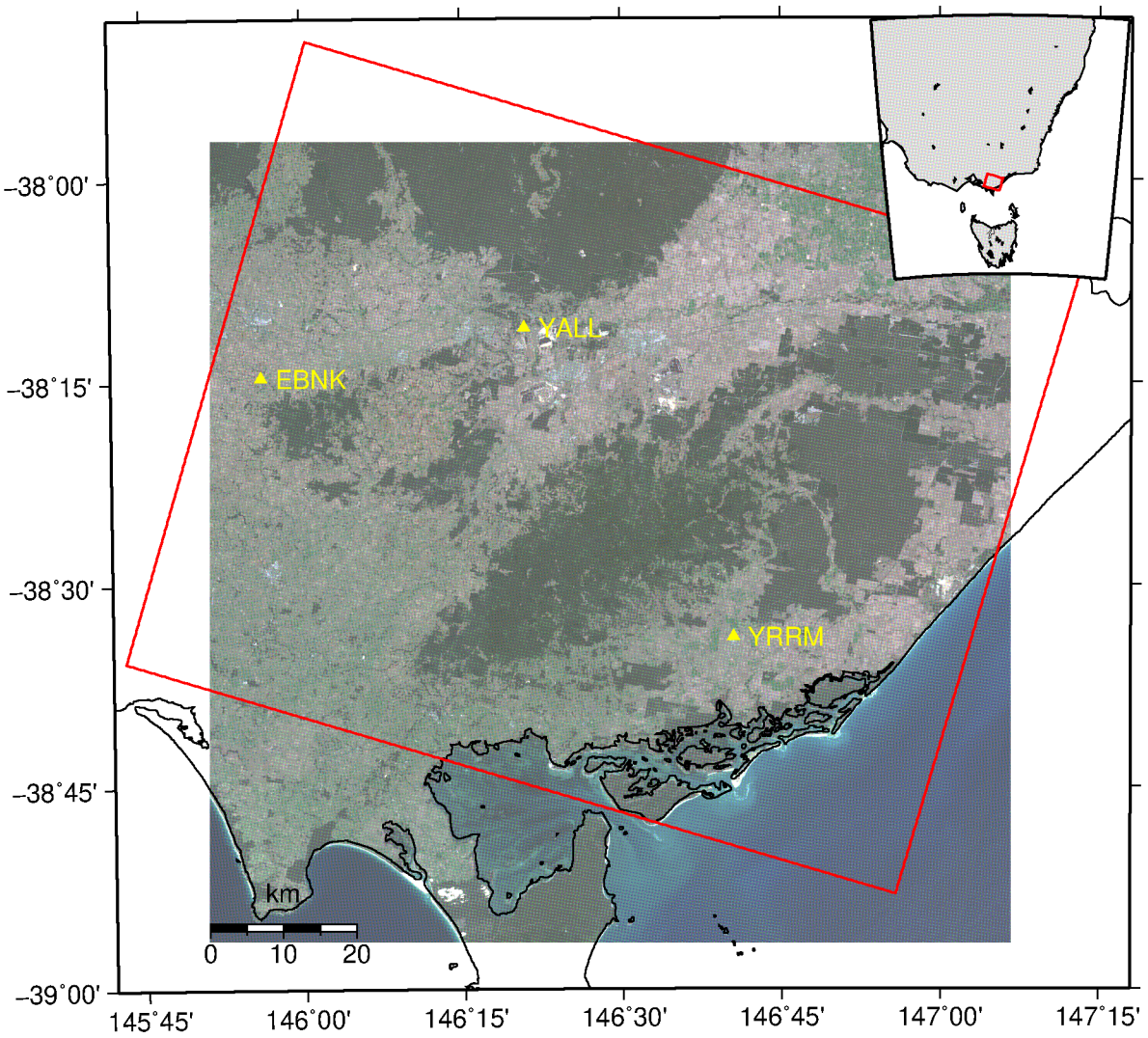

3.1 Study area and data used

Figure 1 shows the study area in the Latrobe Valley with the SAR scene extents in the red rectangle containing three CORS located near Yallourn North (YALL), Ellinbank (EBNK), and Yarram (YRRM). All of these CORS are GNSS antennas mounted on top of buildings, so cannot be verified as stable in the way a deep-seated concrete pillar could be. It is assumed that the motion detected in the GNSS time series reflects the ground motion rather than that of the building structure. Building mounted CORS are increasingly included in global and regional estimates of deformation (e.g., Blewitt et al. 2018), and are the only available CORS in this region. Dual-frequency GPS data at the three sites were processed using Bernese software v5.2 (Dach et al. 2015) by Geoscience Australia in ITRF2014, constrained to seven Australian core IGS stations (G. Hu, 2019, personal communication). The GNSS east and north components were transformed to ITRF2014-Aus by removing the horizontal Australian Plate Model (ICSM 2017). YALL is central to the three sites, and although it has a data gap during the period of InSAR acquisition (Figure 2), it has many nearby

pixels (Figure 3) and is chosen as the reference site for the SCRP connection method. All three CORS were used for PFMC and MCRP.

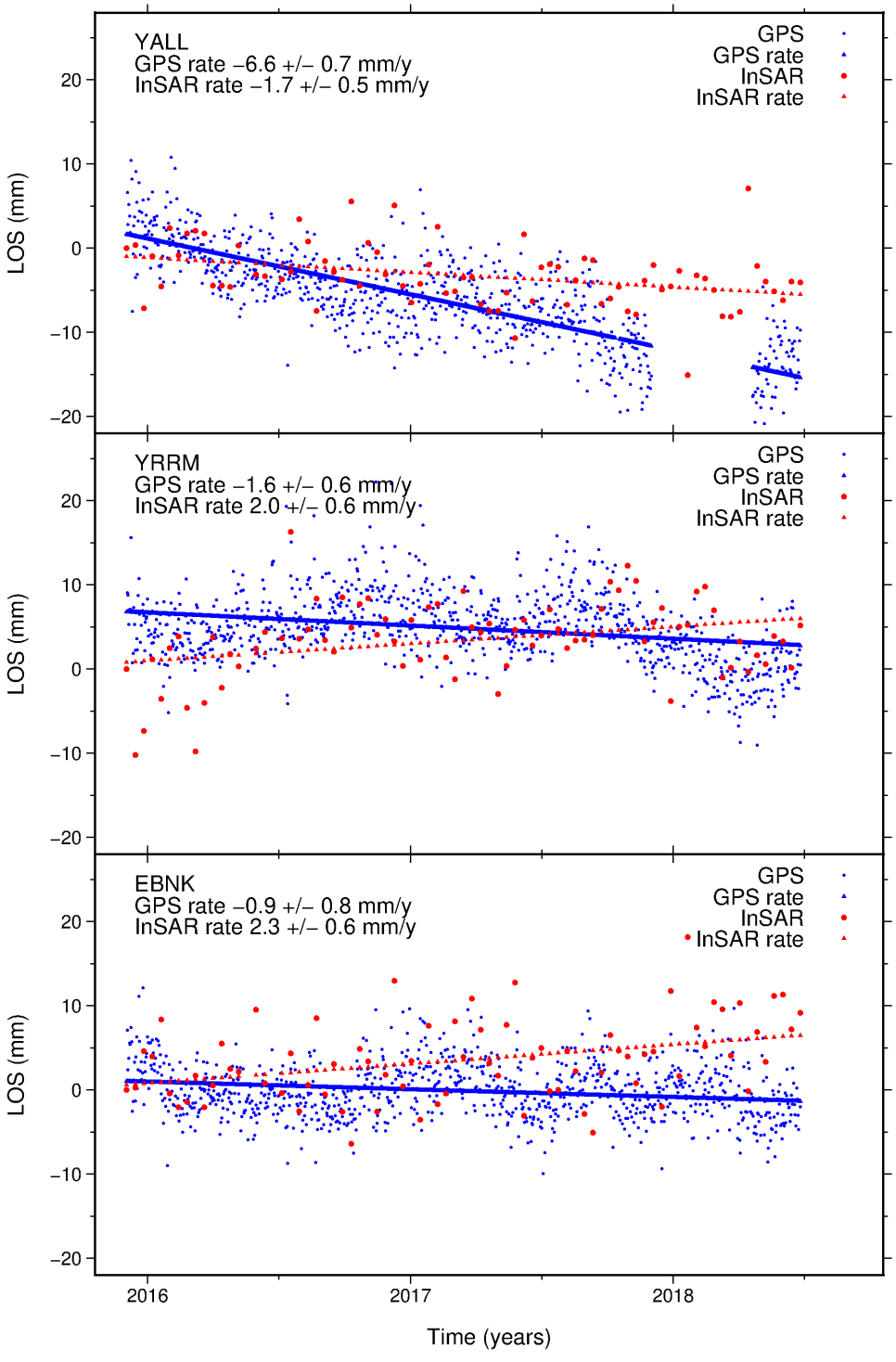

Figure 2: Comparison of 2015.92-2018.57 LOS GNSS (ITRF2014-Aus) and LOS Sentinel-1 (arbitrary reference frame) time series displacements at each CORS. The Sentinel-1 time series RP is an average of the (11, 4, 8) closest InSAR pixels (within 70 m) of the (YALL, YRRM, EBNK) CORS respectively, with the dashed red and solid blue line showing the CATS-derived LOS rate for the Sentinel-1 and GNSS time series respectively. Two offsets were estimated and removed from the YALL GNSS time series in CATS using the complete time series (2011-2019.5), with the rate and uncertainty then re-estimated for the Sentinel-1 time period 2015.92-2018.57 only.

The 77 C-band Sentinel-1 (from the European Space Agency; ESA) descending scenes were processed to generate interferometric products for the period using the GAMMA software (Wegmüller and Werner, 1997). We then used StaMPS to apply the multi-temporal small baseline subset (SBAS) method of Hooper (2008) resulting in slowly decorrelating filtered phase (SDFP) differences. The SBAS SDFP difference matrix was inverted to provide post-processed LOS displacement time series ready for transformation to a TRF. A planar phase ramp was computed for each interferogram independently in StaMPS and removed to mitigate long-wavelength orbital and ionospheric biases.

The GPS daily solutions were then transformed into ITRF2014-Aus East, North and Up coordinate differences. The LOS positions for the 2015.92-2018.57 time series are shown in Figure 2, where the GNSS 3D positions have been transformed to LOS position at the relevant Sentinel-1 incidence angle (θ=40°) and satellite heading (α=193°), as per Section 2.2. The CATS time series estimation software was used to compute 1D GNSS LOS rates (v^G) and uncertainties (σ^G), using a spectral index of -1 (flicker noise), while solving for offsets and annual and semi-annual terms. Figure 2 shows the LOS time series for the GNSS and Sentinel-1, and the modelled trend and offsets. The GNSS time series is LOS in the ITRF2014-Aus, while the Sentinel-1 is shown in an arbitrary datum prior to transformation to the TRF.

3.2 Interpolating to the RP

Connecting the InSAR scene to the TRF is a three-step process, as stated in Section 1 (Introduction), where the first step is to interpolate the InSAR data to the CORS RP using rates v_i^I from the nearest pixel(s). Each of the three methods being tested estimate the InSAR RP v_0^I in different ways. SCRP uses either the single nearest v_i^I (e.g. Filmer et al. 2020) or the average of v_i^I within a given distance; PFMC as used by Fuhrmann et al. (2016) employed OK; Bekaert et al (2017) used the bootstrapping method to interpolate v_0^I for the MCRP method.

Following Section 2.1, using the closest single v_i^I (or multiple v_i^I) to estimate v_0^I relies on the assumption that the motion of the estimated v_0^I is the same, or very close to the true motion of the CORS structure in the arbitrary InSAR reference frame. This assumption is also dependent on the number and proximity of the InSAR pixels adjacent to the CORS. Figure 3 shows the SDFP pixels at each of the CORS for this case study. This indicates that there are gaps around all of them in some directions, and EBNK has few coherent pixels within a radius out to 500 m, which is the criterion for the method of Bekaert et al. (2017). From this, it is clear that the effectiveness of any criterion is site-dependent. Specifically, YALL has a large variation in v_i^I near the CORS possibly due to the nearby (within 1 km) coal mining activity (e.g., Ng et al. 2015). Around YRRM, the v_i^I are more uniform and are likely to be reflections from houses in the town of Yarram. The EBNK CORS is in a rural location surrounded by farmland with few buildings that reflect C-band radar, hence the sparse pixels.

In addition to the number of adjacent pixels, the variation in their v_i^I may also contaminate the TRF connection. Figure 4 shows the v_i^I in Figure 3, but plotted as a function of distance from the RP. YALL RP (Figure 4) demonstrates the possible risk of including large numbers of pixels several hundred metres from the RP, because the variation in v_i^I increases noticeably with distance from YALL. This is likely to be caused by the close proximity of mining activities to YALL, where v_i^I close to the RP are ~ -2 mm/yr, but tend towards uplift at 0.2-0.3 km while indicating subsidence >-5 mm/yr beyond 0.3 km. Acknowledging that taking the average, or better still, the median of these v_i^I

will mitigate the variation, v_0^I may not fully represent the CORS motion which explicitly connects it to the TRF. All three sites have a small variation in v_i^I within 70 m of the CORS, so this distance is chosen for averaging nearby pixels. Table 1 summarises results for four methods for RP v_0^I estimation used for TRF connection, and demonstrates possible errors for each.

Another method of combining multiple v_i^I to determine v_0^I is by using OK (e.g., Fuhrmann et al. 2016). OK estimates of v_0^I at each CORS were determined by first estimating the semivariogram using a spherical model function for circles of radius 5 km (the distance beyond which v_i^I are uncorrelated, cf. Figure 4) on a regular grid across the scene. Additionally, the nugget was constrained to be zero (i.e., at zero distance, the semivariogram should be zero), because if this is not done, the spherical covariance model function does not fit the empirical semivariogram data well in this study. This is likely due to the small number of data points for short distance lags in the semivariogram resulting from sparse InSAR pixel distribution (see Chipeta et al. 2016). By setting the nugget to zero, we were able to derive a more realistic model function. Note that setting the nugget to zero implies a higher weight for data points close to the interpolation location compared to more distant data points and results in a less smooth interpolated surface (Guedes et al. 2020). In our case, OK interpolation is only used to estimate v_0^I, with the objective to derive the most representative value at the CORS, so there is no particular requirement for smoothness compared to neighbouring interpolation locations. In order to derive a statistically rigorous semivariogram model, we use the median of all the semivariogram parameters fitted in the 5 km circles across the scene resulting in the parameters sill=11.13 $(\text{mm/y})^2$, range=600 m (used as "radius" for OK in Table 1). Note that the estimated errors for OK are somewhat larger than for averaging from points closer to the site. The semivariogram (not shown) indicates that v_i^I are correlated over a larger distance than used for the other methods in general, but this is not necessarily the case in the vicinity of the three CORS stations.

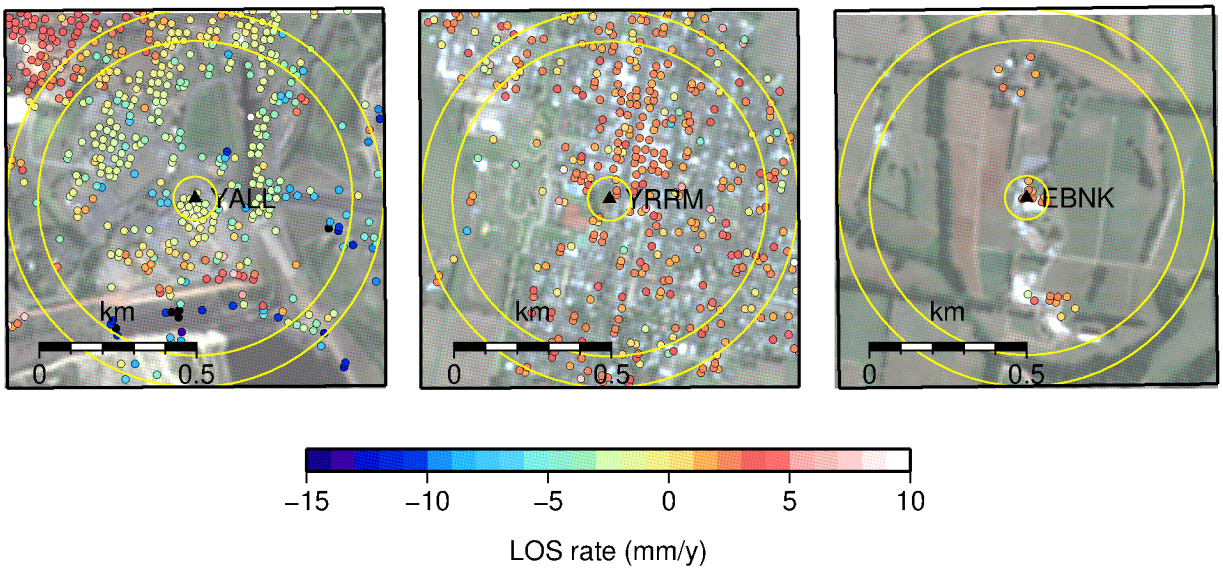

Figure 3: InSAR pixels (coloured circles) in an area of 1 sq. km around YALL, YRRM and EBNK CORS (black triangles). Colours represent the LOS v_i^I in the InSAR reference frame. Circles of radius 70, 500 and 600 m radius are drawn for reference. Background image: Sentinel-2 optical data (RGB channels) acquired on 2017-03-09.

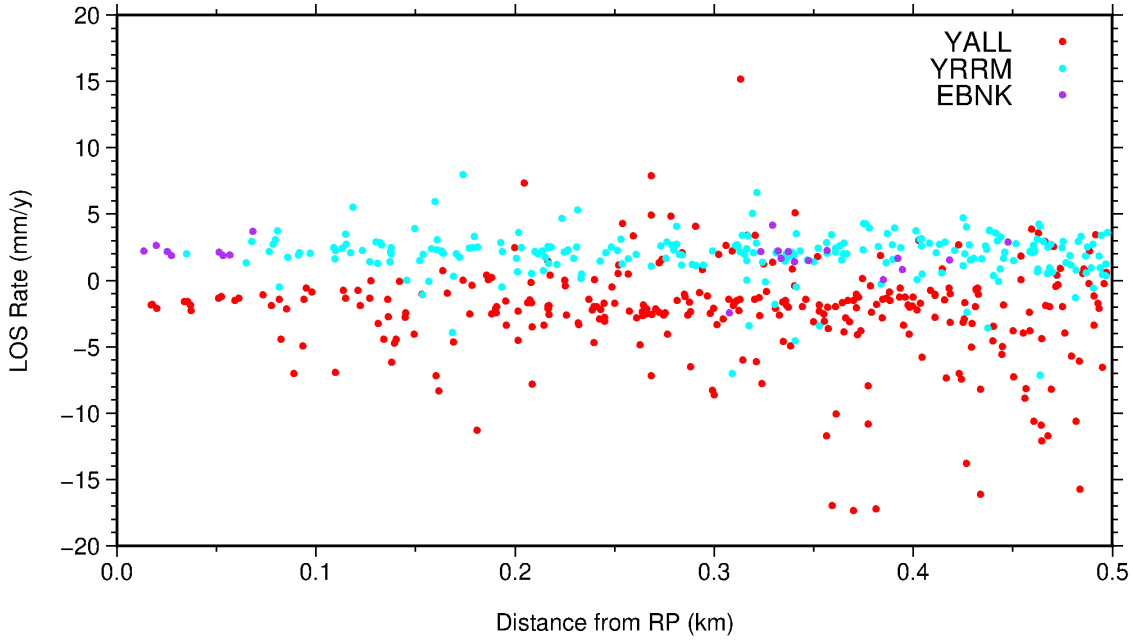

Figure 4: LOS Sentinel-1 v_i^I (before TRF connection) and their change with respect to distance (up to 0.5 km) from the CORS. EBNK (purple dots), YALL (red dots) and YRRM (blue dots).

Table 1 shows that the SCRP differences between the 70 m radius v_0^I and 'nearest pixel' v_0^I are no more than 0.1 mm/yr which is less than the estimated uncertainty, whereas the 500 m radius v_0^I differences are up to 0.65 mm/yr which is more than the estimated uncertainty for the bootstrap method. Over all, the different methods have no more than 0.65 mm/yr difference at YALL, which suggests that v_0^I errors are mostly within uncertainty as determined by the 'nearest pixel' and 70 m radius threshold. OK includes data over a 600 m radius (the estimated range parameter) which although including pixels over a large area, varies weights according to the distance from the RP resulting in maximum differences of less than 0.15 mm/yr compared to the SCRP methods. The difference between the other methods and the bootstrap suggests that the bootstrap σ_0^I may be over-optimistic. Nevertheless, to be consistent with the RP interpolation methods used in the original publications, we used the average within 70 m method for the SCRP method, OK (to 600 m radius) for the PFMC and bootstrap (to 500 m radius) for the MCRP.

Site	GNSS (ITRF2014-Aus	Nearest single pixel (SCRP)	Average within 70 m (SCRP)	Bootstrap 500 m (MCRP)	Ordinary Kriging 600 m (PFMC)
YALL	-6.6 ± 0.7	-1.72 ± 0.53	-1.75 ± 0.53	-2.37 ± 0.22	-1.82 ± 0.98
YRRM	-1.6 ± 0.6	2.09 ± 0.56	2.03 ± 0.62	1.95 ± 0.12	2.18 ±1.18
EBNK	-0.9 ± 0.8	2.19 ± 0.66	2.29 ± 0.65	1.85 ± 0.27	2.21 ± 0.87

Table 1: LOS InSAR v_0^I and σ_0^I (mm/yr) in an arbitrary InSAR reference frame at each CORS using different TRF connection methods. This can be compared with Figure 4 showing the change in pixel rate with respect to distance from the CORS. The GNSS rate v^G and uncertainty σ^G for each CORS from Figure 2 are also shown for comparison.

3.3 Analysis and error propagation of TRF errors for a single RP

Here, we apply error propagation (described in Section 2) to the SCRP transformation to demonstrate the uncertainties that may propagate into the transformed v_i^{SCRP}. This is based on the terms in Eq. (4) (shown as variance $(\sigma_i^I)^2$), but with the estimated uncertainty shown in this section as SD σ_i^I. Figure 5 shows how the errors propagate across the deformation map from the SCRP by applying the different terms in Eq. (4). Figure 5 (top left) shows the spatial variation of time series noise σ_i^I, which comprises turbulent atmospheric error, and also variation in linearity of deformation, such as annual signal, non-linear motion etc. Figure 5 (bottom left) shows $\sigma(v_i^I - v_0^I)$. This error is zero at YALL increasing noticeably within a km or so of YALL. In most parts of the scene, $\sigma(v_i^I - v_0^I) > \sigma_i^I$ due to the contribution of error from the RP. Figure 5 (top right) shows σ^G applied uniformly across the scene. Figure 5 (bottom right) shows σ_i^{SCRP} which is the quadrature sum of $\sigma(v_i^I - v_0^I)$ (bottom left) and σ^G (top right). σ_i^{SCRP} is smallest (~1 mm/yr) close to YALL where the errors are correlated. The uncertainties increase up to ±2 mm/yr away from YALL, exceeding this in the northwest and southwest regions, and also in an area between YALL and YRRM.

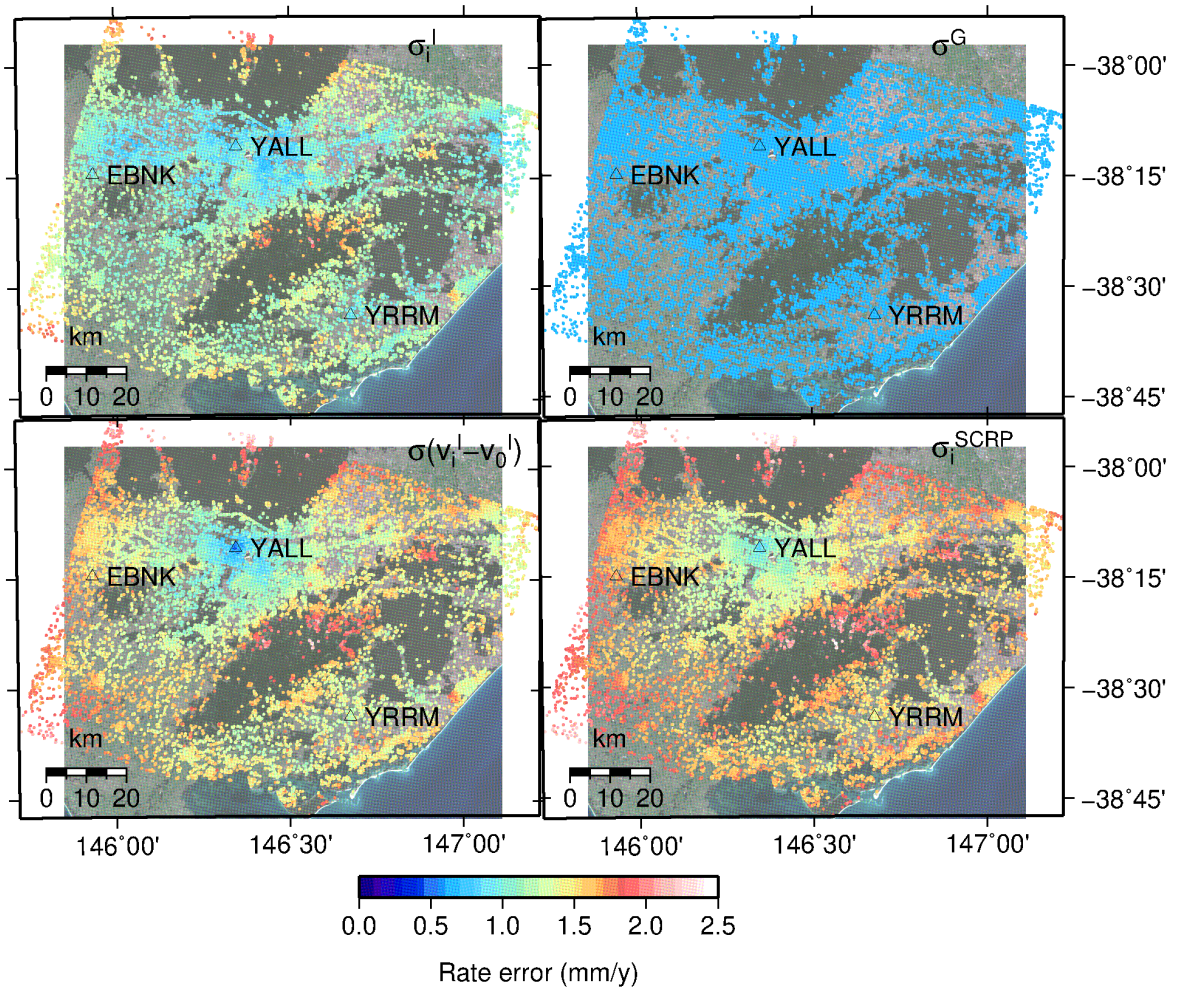

Figure 5: Components of error propagation from Eq. (4). Top left is σ_i^I at each pixel. Bottom left is $\sigma(v_i^I - v_0^I)$ for the YALL RP (which is approximately the quadrature sum of σ_i^I and σ_0^I except near the RP). Top right is the GNSS rate uncertainty at the YALL CORS station. Bottom right is the total error σ_i^{SCRP} as per Eq. (4). Background image: Sentinel-2 optical data (RGB channels) acquired on 2017-03-09.

3.4 Comparison of methods for TRF connection

InSAR v_i^I and associated σ_i^I for each of the three TRF connection methods tested are shown in Figure 6. The SCRP TRF method (Figure 6, SCRP, top) indicates rates between 0 mm/yr and -5 mm/yr for much of the scene, but with subsidence reaching magnitudes larger than -20 mm/yr near YALL and other isolated small areas where the subsidence rate is around -20 mm/yr. The uncertainty map on the top right indicates σ_i^{SCRP} (as per Eq. (4), i.e., the same map as in Fig. 5, bottom right) to be < 1 mm/yr close around the single YALL CORS, but increases towards 2 mm/yr further away from YALL. The reliability of v_i^{SCRP} towards the edge of the scene is dependent on the phase ramp estimated and removed in the processing to mitigate the long-wave orbital and ionospheric errors that can be present in C-band SAR (e.g., Fattahi and Amelung 2014; Gomba et al. 2017). This is a key difference with the PFMC method adopted by Fuhrmann et al. (2015), where the long-wavelength errors are determined by the constraints to multiple CORS. σ_i^{PFMC} is lower than σ_i^{SCRP} near the CORS not used as the RP for the SCRP method, but σ_i^{PFMC} increases away from the CORS sites.

Figure 6 (PFMC right) shows that a small change in the tilt of the plane, while still fitting v_0^I at the CORS sites, produces large σ_i^{PFMC} at the edge of the scene. This effect would be reduced if the CORS sites were more widely distributed with more robust geometry, however, this study area illustrates the challenges of TRF connection where there is a limited number of CORS available, which is often the case for limited area deformation studies. Figure 6 (PFMC left) shows larger magnitude v_i^{PFMC} subsidence in the northeast corner and larger magnitude uplift in the southwest corner (cf. top row of Figure 7). Figure 6 (bottom right) shows that σ_i^{MCRP} are small near the CORS and because the transformation is not extrapolated beyond the specified CORS radius, σ_i^{MCRP} do not increase at the scene edges as per σ_i^{PFMC}. We used a radius of 85 km which is more appropriate for C-band Sentinel-1 whereas Bekaert et al. (2017) chose a radius of 20 km appropriate for the L-band ALOS. The increase in radius is justified because the C-band frequency is 4.3 times higher than the L-band frequency, so the same number of phase cycles that would occur over 20 km for L-band would occur over 4.3 × 20 km for C-band (Fattahi et al. 2017).

A further insight is shown in Figure 7 (bottom left) where v_i^{MCRP} are more positive across the scene than v_i^{SCRP}. This is because the difference between v^G and v_0^I (d_j in Eq. 8) at YALL (-4.9 mm/y) is more negative than at YRRM (-3.5 mm/y) and EBNK (-3.7 mm/y) by >1 mm/yr. Therefore, the difference $v_i^{MCRP} - v_i^{SCRP}$ is less near YALL where the connection to YALL is more heavily weighted (a_{ij} in Eq. (8)), but because the radius from both EBNK and YRRM overlap (and influence) YALL, v_i^{MCRP} is not the same as v_i^{SCRP} at YALL. The difference $v_i^{MCRP} - v_i^{SCRP}$ is also less in the northeast of the scene which is greater than 85 km from EBNK with the discontinuity in $v_i^{MCRP} - v_i^{SCRP}$ evident. Figure 7 (top, right) shows σ_i^{PFMC} - σ_i^{SCRP} is close to zero in the centre of the scene, notably near YRRM and EBNK. Near YALL, σ_i^{PFMC} is slightly higher than σ_i^{SCRP} due to the uncertainty contributions from the other CORS connections. Within 20 to 30 km of YALL, σ_i^{MCRP} is slightly higher than σ_i^{SCRP} for the same reason. σ_i^{PFMC} has larger magnitude than σ_i^{SCRP} near the northeast and southwest edges of the scene.

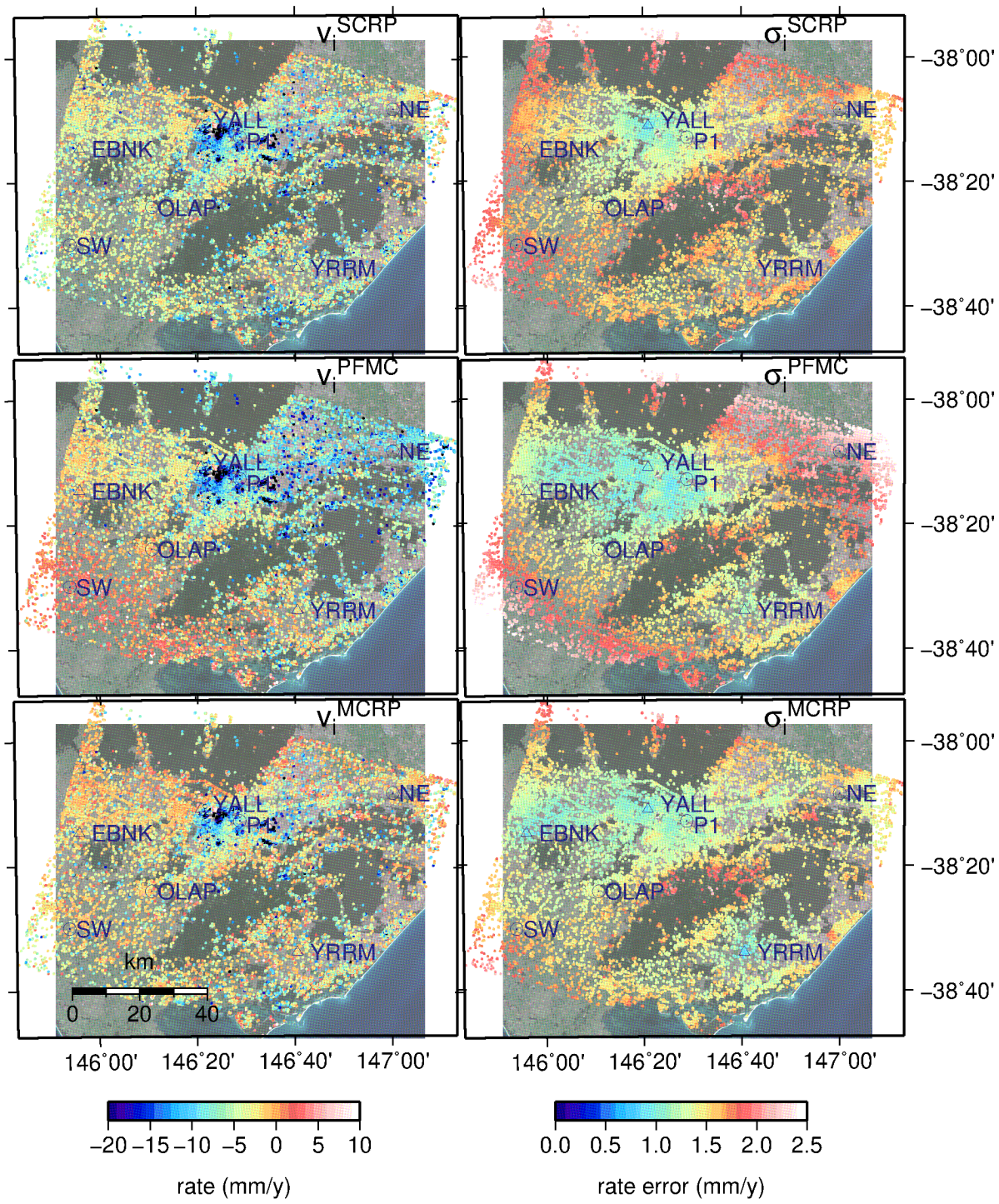

Figure 6: InSAR v_i^I resulting from the three TRF connection methods (left) and their respective σ_i^I propagated through each transformation (right). Background image: Sentinel-2 optical data (RGB channels) acquired on 2017-03-09.

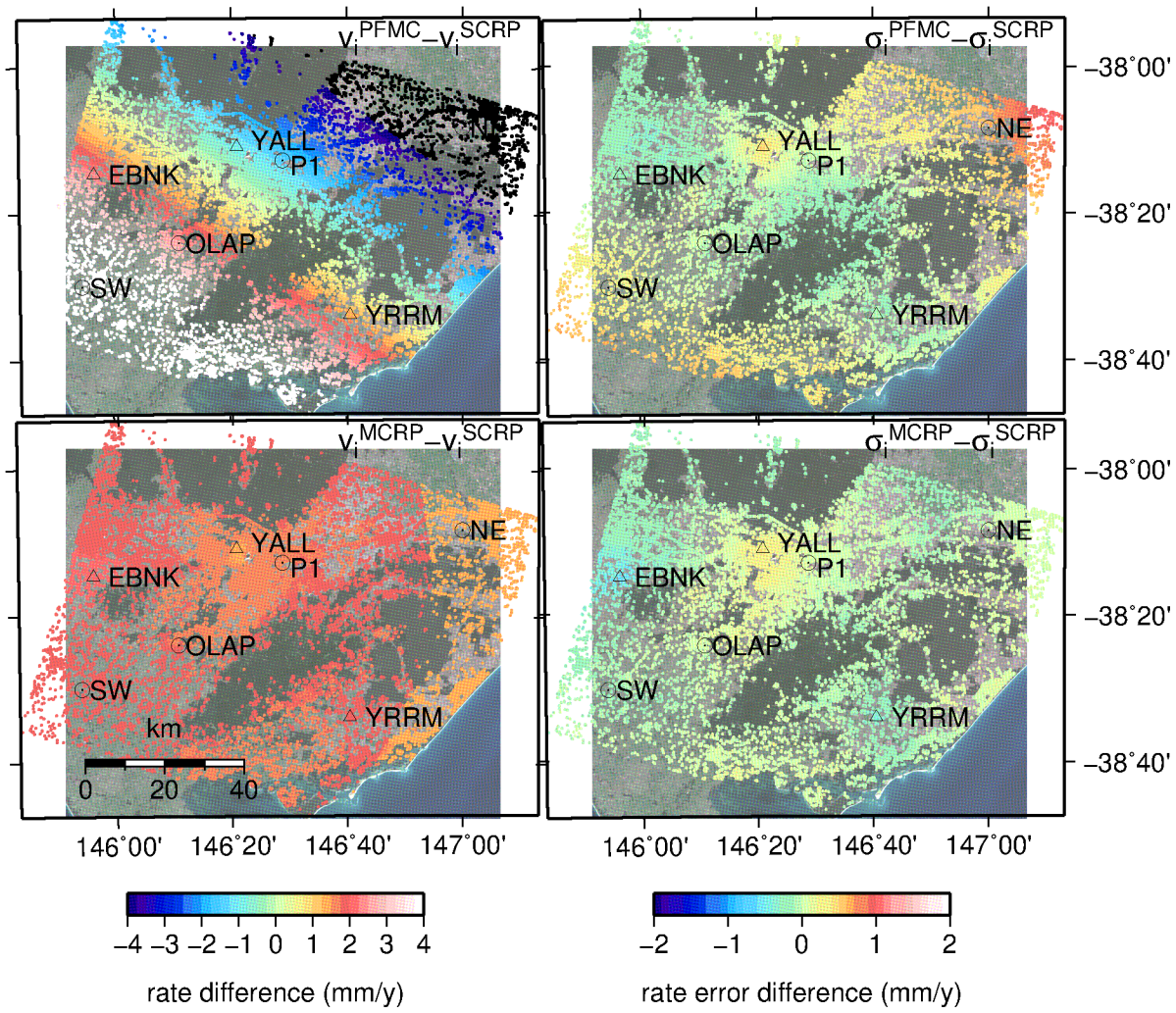

Figure 7: Rate difference $v_i^{PFMC} - v_i^{SCRP}$ (top left) and rate uncertainty difference $\sigma_i^{PFMC} - \sigma_i^{SCRP}$ (top right). Rate difference $v_i^{MCRP} - v_i^{SCRP}$ (bottom left) and rate uncertainty difference $\sigma_i^{MCRP} - \sigma_i^{SCRP}$ (bottom right). Background image: Sentinel-2 optical data (RGB channels) acquired on 2017-03-09.

The differences and similarities between the methods can be seen more clearly in Figure 8 by comparing TRF connected v_i^I from each method at seven locations as shown in Figure 7. At YRRM and EBNK, v_i^{PFMC} and v_i^{MCRP} are similar, while v_i^{SCRP} is from 1.5 to 2 mm/yr larger magnitude because of the larger difference between v_0^I and v^G at YALL. v_i^{PFMC} at sites SW and NE are significantly different from the other two methods, where v_i^{PFMC} is 5 mm/yr higher than v_i^{SCRP} at site SW and 5 mm/y lower than v_i^{SCRP} at site NE (Figures 7 and 8). This is because the plane fit can amplify errors at large distances because they are extrapolated beyond the constraining CORS.

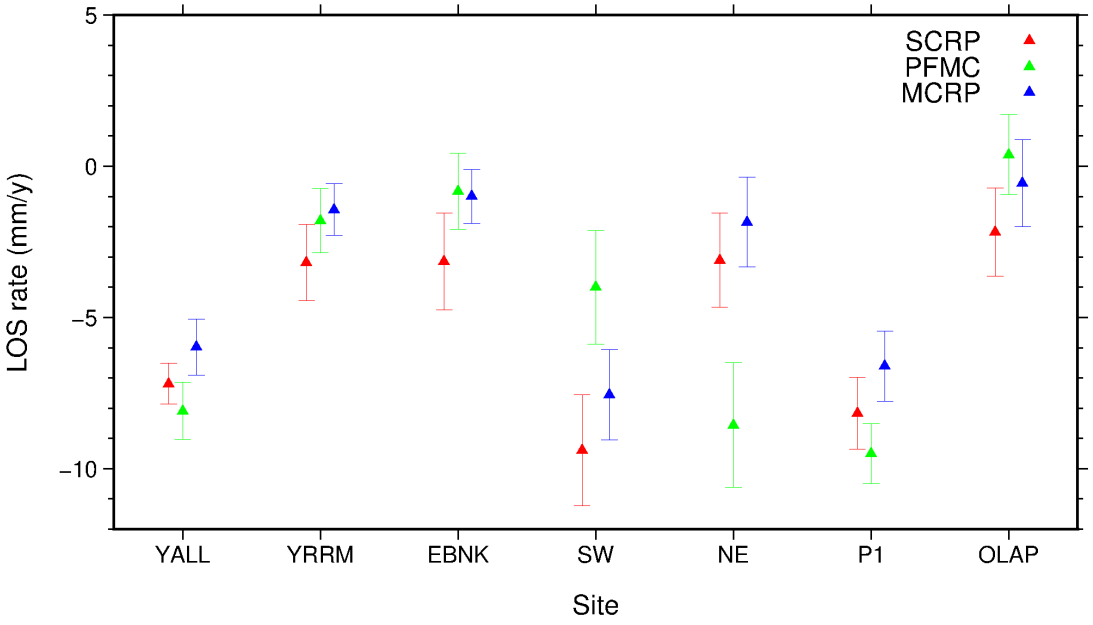

Figure 8: InSAR v_i^I for the sites shown in Figure 7 with error bars indicating their σ_i^I. There are no sites where all three methods have rates within their uncertainties suggesting that the differences among the methods in some locations are statistically significant.

An additional example of the impact from the choice of TRF method is demonstrated when we focus on the coastal region to the east of YRRM. There are sufficient InSAR pixels along this coastline to estimate the VLM (converted from LOS rate using Eq. (13) and assuming zero horizontal rate) in this coastal region. To provide independent comparisons for the InSAR, we used rates calculated from two GNSS campaigns conducted by the Victorian Department of Environment, Land, Water and Planning (DELWP) in 2004 and 2019. The GNSS station locations are shown in Figure 9 (top), with the mean v_i^I from the 10 nearest pixels used for the InSAR comparison (Figure 9, bottom). The relevance of coastal VLM is demonstrated by the impact of relative sea level change when the coast is also subsiding or uplifting (e.g., Mazzotti et al. 2008; Wöppelmann et al. 2013; Featherstone et al. 2015; Bekaert et al. 2017). If the coastal region is subsiding, as suggested in Figure 6 (highlighted in Figure 9), then this will exacerbate the rise in sea level and increase the risk of coastal communities to coastal inundation (Nicholls and Cavenaze 2010; Karegar et al. 2017). We take the mean v_i^I of pixels along the coastal fringe within 7 km of the coast (Figure 9) from each method, with the median of their uncertainty (Table 2). The differences among the mean rates reach 3.6 mm/yr, with the largest mean difference between v_i^{MCRP} and v_i^{PFMC} (cf. Figure 9; all v_i^I are converted to VLM).

Method	SCRP	PFMC	MCRP
Mean v_i^I ± SD (VLM)	-6.5 ± 6.5	-8.3 ± 6.9	-4.7 ± 6.5
Median σ_i^I	1.98	2.23	2.09
Minimum v_i^I (VLM)	-34.9	-39.8	-33.1
Maximum v_i^I (VLM)	20.9	18.8	22.7

Table 2: Descriptive statistics for Sentinel-1 v_i^I (converted to VLM) (cf. Figure 9) for each of the three TRF connection methods. The SD reflects the v_i^I variability across the coastal region, while median σ_i^I is the median of all σ_i^I as shown in Figure 6 (left). Units are mm/yr.

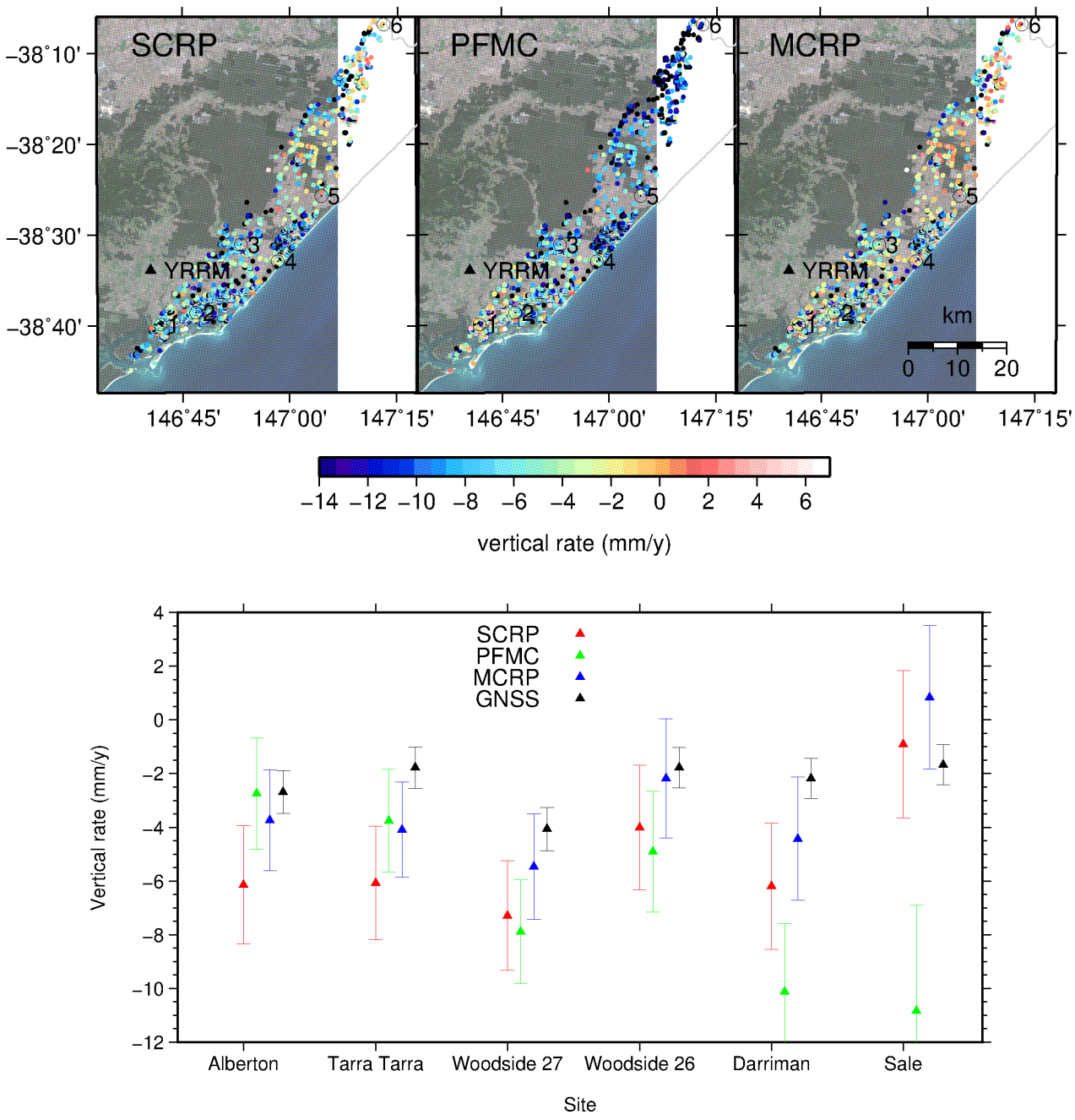

Figure 9: (top) Closer view of the Gippsland coastal region with Sentinel-1 vertical v_i^I from each of the three TRF connection methods. Background image: Sentinel-2 optical data (RGB channels) acquired on 2017-03-09. Campaign GPS sites are numbered in black: 1) Alberton; 2) Tarra Tarra; 3) Woodside 27; 4) Woodside 26; 5) Darriman; 6) Sale. (bottom) TRF transformed Sentinel-1 v_i^I (mean calculated from the nearest 10 pixels converted to vertical assuming zero horizontal velocity) and GNSS rates calculated from the Victorian Department of Environment, Lands, Water and Planning (DELWP) observations in 2004 and 2019 (15 years).

Coastal Sentinel-1 vertical v_i^I are shown in Figure 9, with the pixels mostly sparse over the rural areas, but there are areas of higher backscatter mid-way along the coastline, and to the south that run around the northern edge of the lakes. There are no towns or built-up areas at these locations,

so it is assumed that there are firm areas of dried lake bed or compacted surface that provides additional backscatter. The vertical v_i^I are mostly negative, suggesting subsidence in the region on, and adjacent to the coast, with VLM around -6 mm/yr (the large SD and regional variability notwithstanding). This suggests subsidence at a rate that is larger than both the 1966 - 2009 and 1993 – 2009 sea level change rates of +2.1 ± 0.2 mm/yr and +3.1 ± 0.6 mm/yr respectively estimated from Australian tide gauges by White et al. (2014) and the 3.15 mm/yr (1993-2018) for the temperate Pacific subregion (35°S - 50°S) from satellite altimetry (Karimi and Deng 2020). This means that relative sea level rise along this part of the Gippsland coast may be as large as +9 mm/yr for the 1993 to present period, effectively tripling the rate of geocentric 'absolute' sea level rise for this section of the coastline.

In Table 2 and Figure 9, the different TRF connections provide variable results, although there is also a large spatial variation in rates across the coastal regions. As shown in Figure 7 and Figure 8, there are larger differences that are spatially dependent on the TRF connection method and the geometry of multiple CORS. The GNSS vertical rate, estimated by dividing the change in vertical position by the 15 years between them, are shown at six coastal locations in Figure 9 (site locations in top, GNSS rates at the bottom). While caution is advised when interpreting rates from only two GNSS campaigns conducted 15 years apart, the GNSS rates indicate that there has been subsidence along this section of the coast over the last decade or more. Figure 9 indicates general agreement (mostly within error bars) for the 2004-2019 GNSS and the 2015.92-2018.57 Sentinel-1 v_i^I suggesting that the subsidence has been steady along this section of the coast over the last decade or more. It is notable that the GNSS rates (between 0 mm/yr and -5 mm/yr) at the GNSS observation points in Figure 9 are less than the v_i^I at those GNSS points, suggesting that the subsidence may have increased during the 2015.92-2018.57 period, although this is not conclusive. The GNSS rates appear to be in best agreement with v_i^{MCRP}.

4. Discussion and Conclusions

We have presented three methods for InSAR TRF connection, generalised their equations and propagated their uncertainties through the three TRF steps to account for error sources in this process. From these results in the Latrobe Valley, and the surrounding regions, we can discuss the advantages and disadvantages of these methods, which are summarised in Table 3.

The decision on how many pixels to include in the RP determination, or method of spatial interpolation when using multiple pixels was not conclusive from Table 1, although it is logical to consider that closer pixels will best represent the motion of the CORS structure. It is important to restate that the objective of TRF connection at CORS is to determine the InSAR rate of the CORS structure, so as to achieve an accurate transformation to the TRF as determined by the GNSS rate at the CORS. The RP connection is site dependent, and the important factors for connecting each CORS are: how many coherent pixels are close to the RP, how large is the range of pixel rates close to the RP, or is the area at or around the site rapidly deforming and different from the CORS? Figures 3 and 4 suggest that apart from YALL, the rates at other CORS were relatively stable, so in these cases the method used is not that critical.

An analysis of each site is essential, because it is necessary to use a method that best suits each particular site. Hence, in the absence of corner reflectors or transponders at RPs, caution is advised using a large radius such as bootstrap over 500 m, or OK over the estimated range (600 m for Sentinel-1) because in some cases this may not reflect the deformation rates of the CORS

structure. Likewise, the use of a single pixel should be verified by surrounding pixels to confirm that this is not an outlier. So, while the OK and bootstrap method over a larger radius may be a more robust estimate of the InSAR rate over the chosen area, it may not be representative of the rate at the CORS. An option is to reduce the radius for the bootstrap method or adapt the covariance model used for OK to suit the characteristics of the RP site.

Method	**Advantage**	**Disadvantage**	**When to use**	**Deformation type**
SCRP	• Simplicity of computation • Transformation is constant in space • Other CORS can be used for validation	• Deterioration in reliability with distance from single CORS • May induce an offset in rates at other CORS	• Small area of interest. • Only one available CORS with reliable GNSS time series, or for independent validation at nearby CORS	• More suitable for local rapid deformation.
PFMC	• Utilises multiple CORS for robust TRF connection. • Transformation is smooth in space	• Extrapolating outside the region bounded by the RPs can exacerbate errors • Unreliable connection at one CORS may introduce a tilt in InSAR rates. • Weak CORS geometry may cause a tilt across the study area.	• Large study area with multiple CORS in a robust network geometry across the full study area. • Region of interest is within the area bounded by the RPs	• For use over large regions where the long-wavelength deformation is linear (constant) in time.
MCRP	• Utilises multiple CORS for robust TRF connection. • Fits well at all RPs	• Transformation is discontinuous in space • Limited by distance from CORS, but dependent on SAR wavelength, so may not cover full region.	• When a dense CORS network is available so that the radius from each CORS overlaps, avoiding gaps in InSAR coverage.	• Suitable where there is variable deformation over short temporal and spatial scales so that each CORS can constrain the local deformation.

Table 3: Summary of advantages and disadvantages of each method and the recommended situation in which each should be used.

The comparisons among the three TRF methods in the case study demonstrates the characteristics of each method. The first point is that the results of each of these are relatively similar, but closer inspection in Figures 7 and 8 indicate differences compared to the SCRP in some places in the study area approaching +5 mm/yr and -5 mm/yr for the PFMC, and up to + 2 mm/yr for

the MCRP. The differences are spatially dependent, and relate to the geometry of the multiple CORS and how the TRF transformations connect to these in the context of the deformation varying in space and time. Comparisons at different points in the scene in Figure 8 show that there is no station where all three methods agree within their uncertainty. The difference at YALL for SCRP is due to the larger difference between the InSAR and GNSS rate at YALL compared with the other two CORS. SCRP and MCRP have the best agreement at most locations although these are not all within their uncertainty, and the MCRP rates generally are larger. Both SCRP and MCRP are significantly different (by more than their uncertainty estimate) from PFMC near the edges of the scene due to the geometry of the CORS and their effect on the fitted plane. The MCRP method was in best agreement with the campaign GNSS data along the coastal areas shown in Figure 9. This assessment of the TRF connection methods relies on the error propagation equations developed in Section 2, highlighting the importance of considering the error contributions to the transformed rates within the specified TRF.

We conclude that the MCRP method appears more reliable than SCRP and PFMC because it is less sensitive to the geometry of the available CORS and may be a pragmatic solution for many study areas with multiple CORS. However, the MCRP can be limited in spatial coverage due to long-wavelength errors, so that the PFMC may be a suitable alternative over larger areas with larger spacings between CORS, provided that the CORS are evenly spaced across the full scene. The SCRP method may be suitable over smaller areas where long wavelength errors are effectively mitigated in the InSAR processing. An additional consideration for choice of TRF connection is the characteristics of the deformation field (cf. Table 3, column 4). For example, the SCRP appears better suited to deformation that has large spatial and temporal variations, because it is constrained in only one place so is less likely to introduce a bias or tilt from multiple CORS connection that are undergoing different deformation. The MCRP also appears suitable for deformation fields with rates that vary in time and space because the local deformation field is connected to the local CORS RP. However, care should be taken at overlap regions which may introduce discontinuities, or introduce a bias at neighbouring CORS. The PFMC is best suited to small magnitude, constant rate deformation where the CORS RPs can mitigate long wavelength InSAR errors and constrain the rates to the steady deformation.

A further comparison was made at the coastal region of southeast Australia. The results from all three TRF methods indicate average subsidence of ~-6 mm/yr. This is a significant finding itself, as it is larger than 'absolute' regional sea level rise, and suggests a relative sea level rise of ~+9 mm/yr, and should be considered when planning for future sea level inundation of the coastal region (e.g., Ramm et al. 2018). However, these rates should be viewed with some caution and be considered an upper bound given that both the Sentinel-1 and GNSS rates at the DELWP GNSS sites were generally less than the mean Sentinel-1 rates of -6 mm/yr across the coastal region. Slow subsidence of a few mm/yr is found across the study region in relation to ITRF2014-Aus, which generally agrees with the study of Ng et al. (2015) using four years of ALOS PALSAR data (2007-2011), which although referenced to a limited area of assumed stable land, suggests that the 2007-2011 rates are continuing through to 2018.5. The relative sea level comparison highlights the importance of the few mm/yr difference at some locations, because this may directly impact the observed magnitude of relative sea level change. Importantly, the rates are referenced to a TRF (ITRF2014-Aus for this study) so can be compared to other sea level studies within the same TRF (cf. Wöppelmann et al. 2009), and assessed in terms of the uncertainties propagated through the transformation process.

Acknowledgements

This research was performed under FrontierSI research project (FSI-4001) funded by the Victorian Department of Environment, Land, Water and Planning (DELWP) and the New South Wales Department of Customer Service (NSW DCS). MF and PJ were supported by FrontierSI project FSI-4001. TF publishes with the permission of the CEO, Geoscience Australia (GA).

The authors would like to both thank and acknowledge the contributions made by all FSI-4001 partners involved in developing, reviewing and supporting the FrontierSI research project, including DELWP, NSW DCS, GA, Land Information New Zealand and Position++, all of which made the research contained in this manuscript possible.

The authors would like to thank Dr Guorong Hu (GA) for re-processing the GNSS data. The authors also thank the European Space Agency for making available the Sentinel-1 InSAR scenes and Sentinel-2 images used as background in the figures.

We would also like to thank Professor Andy Hooper for making StaMPS software freely available. All figures were plotted using the Generic Mapping Tools (Wessel et al., 2013).

The authors thank the four reviewers (three anonymous and Dr Xavier Collilieux), and Associate Editor Professor Crespi for their constructive reviews that have helped us to improve the manuscript.

Author contribution statement

PJ and MF designed the TRF connection experiment, analysed the data and wrote the paper. PJ performed the computations. TF processed the Sentinel-1 SAR data, post-processed the GNSS rates, and contributed to editing the manuscript.

Data availability statement

Sentinel-1 data used in this paper is freely available from ESA and was queried and downloaded using the SARA hub (Sentinel Australasia Regional Access, see https://copernicus.nci.org.au/sara.client).

The three GNSS CORS used in this paper are operated by DELWP. GNSS RINEX (Receiver INdependent Exchange format) data is freely available from the Geoscience Australia GNSS data repository (see https://data.gnss.ga.gov.au/).

Campaign GNSS data for the Gippsland coast has been made available from DELWP on request.

References

Altamimi Z, Rebischung P, Métivier L, Collilieux X (2016) ITRF2014: A new release of the International Terrestrial Reference Frame modeling nonlinear station motions, J. Geophys. Res. Solid Earth, 121:6109– 6131, doi:10.1002/2016JB013098.

Baarda W (1981) S-transformations and criterion matrices, *Publications on Geodesy, New Series*, vol 5, 2nd edn. Netherlands Geodetic Commission, Delft

Bähr H, Hanssen RF (2012) Reliable estimation of orbit errors in spaceborne SAR interferometry: the network approach. Journal of Geodesy, 86:1147-1164, doi: 10.1007/s00190-012-0571-6

Bekaert DPS, Hooper A, Wright TJ (2015a) A spatially variable power-law tropospheric correction technique for InSAR data. *Journal of Geophysical Research: Solid Earth*, 120(2):1345−1356, doi:10.1002/2014JB011558.

Bekaert DPS, Hooper A, Wright TJ (2015b) Reassesing the 2006 Guerrero slow slip event, Mexico: implications for large earthquakes in the Guerrero Gap, *Journal of Geophysical Research: Solid Earth*. 120: 1357–1375, doi:10.1002/2014JB011557.

Bekaert DPS, Hamlington BD, Buzzanga B, Jones CE (2017) Spaceborne synthetic aperture radar survey of subsidence in Hampton Roads, Virginia (USA). *Science Reports*, 7: 14752, doi:10.1038/s41598-017-15309-5.

Bell, J. W., Amelung, F., Ferretti, A., Bianchi, M., & Novali, F. (2008). Permanent scatterer InSAR reveals seasonal and long-term aquifer-system response to groundwater pumping and artificial recharge. Water Resources Research, 44:W02407. https://doi.org/10.1029/2007WR006152

Blewitt G, Lavallée (2002) Effect of annual signals on geodetic velocity, *Journal of Geophysical Research*, 107(B7):2145, doi:10.1029/2001JB000570.

Blewitt G, Hammond WC, Kreemer C (2018) Harnessing the GPS data explosion for interdisciplinary science, *EOS – Transactions of the American Geophysical Union,* 99, doi: 10.1029/2018EO104623.

Brooks BA, Merrifield MA, Foster J, Werner CL, Gomez F, Bevis M, Gill S (2007) Space geodetic determination of spatial variability in relative sea level change, Los Angeles basin. *Geophysical Research Letters*, 34(1):L01611, doi:10.1029/2006GL028171.

Bui LK, Featherstone WE, Filmer MS (2020) Disruptive influences of residual noise, network configuration and data gaps on InSAR-derived land motion rates using the SBAS technique, *Remote Sensing of Environment*, 247(111941), https://doi.org/10.1016/j.rse.2020.111941

Cao·Y, Li Z, Wei·J, Hu J, Duan M, Feng G (2018) Stochastic modeling for time series InSAR: with emphasis on atmospheric effects. *Journal of Geodesy,* 92(2):185–204, doi.org/10.1007/s00190-017-1055-5

Chang L, Hanssen RF (2016) A probabilistic approach for InSAR time series postprocessing. IEEE Trans Geosci Remote Sens 54(1):421–430. doi:10.1109/TGRS.2015.2459037.\

Chipeta M, Terlouw D, Phiri K, Diggle P (2016) Inhibitory geostatistical designs for spatial prediction taking account of uncertain covariance structure. Environmetrics 28: e2425, DOI 10.1002/env.2425

Collilieux X, Altamimi Z, Argus DF, Boucher C, Dermanis A, Haines BJ, Herring TA, Kreemer C, Lemoine FG, Ma C, MacMillan DS, Makinen J, Métivier,L, Ries JC, Teferle FN, Wu X (2014) External evaluation of the Terrestrial Reference Frame: report of the task force of the IAG sub-commission 1.2, Proceedings of the IAG General Assembly, Melbourne, Australia, June 28 - July 2, 2011, Chris Rizos and Pascal Willis Ed., vol. 139, pp. 197-202, International Association of Geodesy Symposia, Springer Berlin Heidelberg, doi:10.1007/978-3-642-37222-3_25

Dach R, Lutz S, Walser P, Fridez P (2015) *Bernese GNSS Software Version 5.2 (User manual)*. Bern Open Publishing. http://dx.doi.org/10.7892/boris.72297

Dheenathayalan P, Small D, Schubert A, Hanssen RF (2016) High-precision positioning of radar scatterers. Journal of Geodesy, 90:403–422, DOI 10.1007/s00190-015-0883-4

Fattahi H, Amelung F (2014) InSAR uncertainty due to orbital errors. *Geophysical Journal International,* 199(1)**:** 549–560, doi: 10.1093/gji/ggu276.

Fattahi H, Simons M, Agram P (2017) InSAR Time-Series Estimation of the Ionospheric Phase Delay: An Extension of the Split Range-Spectrum Technique. *IEEE Transactions on Geoscience and Remote Sensing*, 55(10): 5984-5996, doi: 10.1109/TGRS.2017.2718566.

Ferretti A, Prati C, Rocca F (2001) Permanent scatterers in SAR Interferometry. *IEEE Transactions on Geoscience and Remote Sensing*, 39(1): 8-20, doi: 10.1109/36.898661

Featherstone WE, Penna NT, Filmer MS, Williams SDP (2015) Nonlinear subsidence at Fremantle, a long-recording tide gauge in the Southern Hemisphere. J. Geophys. Res.: Oceans 120(10):7004−7014. https://doi.org/10.1002/2015JC011295.

Fialko Y, Simons M, Agnew D (2001) The complete (3-D) surface displacement field in the epicentral area of the 1999 MW7.1 Hector Mine Earthquake, California, from space geodetic observations. *Geophys. Res. Lett.*, 28: 3063–3066.

Filmer MS, Williams SPD, Hughes CW, Wöppelmann G, Featherstone WE, Woodworth PL, Parker AL (2020) An experiment to test satellite radar interferometry-observed geodetic ties to remotely monitor vertical land motion at tide gauges. *Global and Planetary Change*, 185:103084, doi.org/10.1016/j.gloplacha.2019.103084

Fuhrmann T, Westerhaus M, Zippelt K, Heck B (2014) Vertical displacement rates in the Upper Rhine Graben area derived from precise levelling. *Journal of Geodesy*, 88(8):773-787

Fuhrmann T, Caro Cuenca M, Knöpfler A, van Leijen FJ, Mayer M, Westerhaus M, Hanssen RF, Heck B (2015) Estimation of small surface displacements in the Upper Rhine Graben area from a combined analysis of PS-InSAR, levelling and GNSS data. *Geophys. J. Int*., 203:614–631.

Fuhrmann, T (2016) Surface Displacements from Fusion of Geodetic Measurement Techniques Applied to the Upper Rhine Graben Area. PhD Dissertation, Karlsruhe Institute of Technology, Karlsruhe, Germany, http://dx.doi.org/10.5445/IR/1000056073

Fuhrmann T, Garthwaite M, Lawrie S, Brown N (2018) Combination of GNSS and InSAR for Future Australian Datums. In: *Proceedings of the Australia IGNSS Symposium 2018*, Sydney, Australia 7 – 9 February 2018 http://www.ignss2018.unsw.edu.au/sites/ignss2018/files/u80/Papers/IGNSS2018_paper_17.pdf

Fuhrmann T, Garthwaite MC (2019) Resolving Three-Dimensional Surface Motion with InSAR: Constraints from Multi-Geometry Data Fusion. *Remote Sens*., 11:241, doi:10.3390/rs11030241

Garthwaite M (2017) On the design of radar corner reflectors for deformation monitoring in multi-frequency InSAR. *Remote Sensing*, 9(7): 648, doi:10.3390/rs9070648.

Gomba G, González FR, De Zan F (2017) Ionospheric Phase Screen Compensation for the Sentinel-1 TOPS and ALOS-2 ScanSAR Modes. IEEE Transactions on Geoscience and Remote Sensing, 55(1): 223-235, doi: 10.1109/TGRS.2016.2604461

Guedes LPC, Bach RT, Uribe-Opazo MA (2020) Nugget effect influence on spatial variability of agricultural data. Engenharia Agrícola, Jaboticabal, 40(1):96-104, doi: http://dx.doi.org/10.1590/1809-4430-Eng.Agric.v40n1p96-104/2020

Hanssen RF (2001). *Radar Interferometry: Data Interpretation and ErrorAnalysis*, Kluwer, Academic.

Hammond WC, Blewitt G, Kreemer C (2016) GPS imaging of vertical land motion in California and Nevada: Implications for Sierra Nevada uplift. *Journal of Geophysical Research - Solid Earth*, 121: 7681–7703, doi: 10.1002/2016JB013458.

Hammond WC, Burgette RJ, Johnson KM, Blewitt G. (2018) Uplift of the Western Transverse Ranges and Ventura Area of Southern California: A four-technique geodetic study combining GPS, InSAR, levelling, and tide gauges *Journal of Geophysical Research - Solid Earth*, 123(1): 836–858, doi: 10.1002/2017JB014499.

Hooper A, Segall P, Zebker H (2007) Persistent scatterer interferometric synthetic aperture radar for crustal deformation analysis, with application to Volcán Alcedo, Galápagos. Journal of Geophysical Research, 112:B07407, doi:10.1029/2006JB004763, 2007

Hooper A (2008) A multi-temporal InSAR method incorporating both persistent scatterer and small baseline approaches. *Geophysical Research Letters*, 35(16):L16302, doi: 10.1029/2008GL034654.

Hooper A, Bekaert D, Spaans K, Arikan M (2012), Recent advances in SAR interferometry time series analysis for measuring crustal deformation. *Tectonophysics*, 514–517: 1−13, doi:10.1016/j.tecto.2011.10.013.

ICSM (2017) Geocentric Datum of Australia 2020 Technical Manual Version 1.2. 2017, Intergovernmental Committee on Surveying and Mapping (ICSM): Australia.

Kampes, B. M. (2006). Radar Interferometry: Persistent Scatterer Technique. Springer, Dordrecht, The Netherlands.

Karegar MA, Dixon TH, Malservisi R, Kusche J, Engelhart SE (2017) Nuisance Flooding and Relative Sea-Level Rise: the Importance of Present-Day Land Motion. Science Reports, 7: 11197, doi:10.1038/s41598-017-11544-y

Karimi AA, Deng, X (2020) Estimating sea level rise around Australia using a new approach to account for low frequency climate signals. *Advances in Space Research,* 65:2235-2238, doi:10.1016/j.asr.2020.02.002.

Liang C, Agram P, Simons M, Fielding EJ (2019) Ionospheric Correction of InSAR Time Series Analysis of C-band Sentinel-1 TOPS Data. *IEEE Transactions on Geoscience and Remote Sensing*, 57(9): 6755-6773, doi: 10.1109/TGRS.2019.2908494.

Mahapatra P, Samiei-Esfahany S, van der Marel H, Hanssen R (2014) On the Use of Transponders as Coherent Radar Targets for SAR Interferometry. *IEEE Transactions on Geoscience and Remote Sensing*, 52(3): 1869, doi: 10.1109/TGRS.2013.2255881.

Mahapatra P, van der Marel H, van Leijen F, Samiei-Esfahany S, Klees R, Hanssen R (2018) InSAR datum connection using GNSS-augmented radar transponders. *Journal of Geodesy,* 92(1):21–32, doi:10.1007/s00190-017-1041-y.

Mazzotti S, Jones C, Thomson RE (2008) Relative and absolute sea level rise in western Canada and northwestern United States from a combined tide gauge-GPS analysis. J. Geophys. Res. - Oceans 113(C11019) https://doi.org/10.1029/ 2008JC004835.

Murray KD, Bekaert DPS, Lohman RB (2019) Tropospheric corrections for InSAR: Statistical assessments and applications to the Central United States and Mexico. *Remote Sensing of Environment*, 232:111326, https://doi.org/10.1016/j.rse.2019.111326

Ng AHM, Ge LL, Li XJ (2015) Assessments of land subsidence in the Gippsland Basin of Australia using ALOS PALSAR data. *Remote Sens Environ*, 159:86–101. https://doi.org/10.1016/j.rse.2014.12.003

Nicholls RJ, Cazenave A (2010) Sea level change and the impacts in coastal zones. *Science*, 328: 1517–1520.

Parker AL, Featherstone WE, Penna NT, Filmer MS, Garthwaite MC (2017) Practical Considerations before Installing Ground-Based Geodetic Infrastructure for Integrated InSAR and cGNSS Monitoring of Vertical Land Motion, *Sensors*, 17:1753, doi:10.3390/s17081753

Parker AL, McCallum L, Featherstone WE, McCallum JN, Haas R (2019) The Potential for Unifying Global-Scale Satellite Measurements of Ground Displacements Using Radio Telescopes, *Geophysical Research Letters* 46(21), 11841-11849

Poitevin C, Wöppelmann G, Raucoules D, Le Cozannet G, Marcos M, Testut L (2019) Vertical land motion and relative sea level changes along the coastline of Brest (France) from combined space-borne geodetic methods *Remote Sensing of Environment*, 222: 275-285, doi:10.1016/j.rse.2018.12.035

Press WH, Flannery BP, Teukolsky SA, Vetterling WT (1986) *Numerical Recipes*. Cambridge University Press, Cambridge.

Ramm TD, Watson CS, White CJ (2018) Strategic adaptation pathway planning to manage sea-level rise and changing coastal flood risk. *Environmental Science and Policy*, 87:92-101, https://doi.org/10.1016/j.envsci.2018.06.001

Raucoules D, Le Cozannet G, Wöppelmann G, de Michele M, Gravelle M, Daag A, Marcos M (2013) High nonlinear urban ground motion in Manila (Philippines) from 1993 to 2010 observed by DInSAR: implications for sea-level measurements. *Remote Sensing of Environment*, 139:386-397, doi:10.1016/j.rse.2013.08.021.

Riddell A., King MA, Watson CS, Sun Y, Riva REM, Rietbroek R (2017) Uncertainty in geocenter estimates in the context of ITRF2014. J. Geophys. Res. Solid Earth, 122:4020–4032, doi:10.1002/2016JB013698.Wegmüller, U.; Werner, C. GAMMA SAR processor and interferometry software. In Proceedings of Third ERS Symposium on Space at the service of our Environment, Florence, Italy, 14-21 March, 1997.

Wegmüller U, Werner C (1997) GAMMA SAR processor and interferometry software. Third ERS Scientific Symposium, Florence, Italy, 17-21 March 1997.

Wessel P, Smith WHF, Scharroo R, Luis J, Wobbe F (2013) Generic Mapping Tools: Improved Version Released. Eos, Transactions, American Geophysical Union, 94(45):409–420, https://doi.org/10.1002/2013EO450001

White NJ, Haigh ID, Church JA, Koen T, Watson CS, Pritchard TR, Watson PJ, Burgette RJ, McInnes KL, You Z-J (2014) Australian sea levels—trends, regional variability and influencing factors. Earth Sci. Rev., 136: 155-174, doi:10.1016/j.earscirev.2014.05.011

Williams S, Bock Y, Fang P (1998) Integrated satellite interferometry: Tropospheric noise, GPS estimates and implications for interferometric synthetic aperture radar products, *Journal of Geophysical Research –Solid Earth*, 103(B11): 27,051–27,067, doi:10.1029/98JB02794.

Williams SDP (2003a) The effect of coloured noise on the uncertainties of rates estimated from geodetic time series. Journal of Geodesy 76(9–10):483–494

Williams SDP (2003b) Offsets in Global Positioning System time series. *Journal of Geophysical Research*, 108(B6): 2310, doi:10.1029/2002JB002156, 2003

Williams, SDP. (2008), CATS: GPS coordinate time series analysis software, *GPS Solutions*, 12(2), 147-153, doi: 10.1007/s10291-007-0086-4.

Wöppelmann G, Le Cozannet G, De Michele M, Raucoules D, Cazenave A, Garcin M, Hanson S, Marcos M, Santamaria-Gomez A (2013) Is land subsidence increasing the exposure to sea level rise in Alexandria, Egypt? Geophys. Res. Lett. 40(12), 2953–2957. https://doi.org/10.1002/grl.50568.

Wöppelmann G, Letretel C, Santamaría A, Bouin MN, Collilieux X, Altamimi Z, Williams S, Martín Míguez B (2009) Rates of sea level change over the past century in a geocentric reference frame. Geophys Res Lett 36(L12607). doi:10.1029/2009GL038720

Wright TJ, Parsons BE, Lu Z (2004) Toward mapping surface deformation in three dimensions using InSAR. *Geophys. Res. Lett.* 31.